GEOCHEMISTRY

How temperature-dependent silicate weathering acts as Earth's geological thermostat

S. L. Brantley[1,2]*, Andrew Shaughnessy[2], Marina I. Lebedeva[1]†, Victor N. Balashov[1]†

Earth's climate may be stabilized over millennia by solubilization of atmospheric carbon dioxide (CO_2) as minerals weather, but the temperature sensitivity of this thermostat is poorly understood. We discovered that the temperature dependence of weathering expressed as an activation energy increases from laboratory to watershed as transport, clay precipitation, disaggregation, and fracturing increasingly couple to dissolution. A simple upscaling to the global system indicates that the temperature dependence decreases to ~22 kilojoules per mole because (i) the lack of runoff limits weathering and retains base metal cations on half the land surface and (ii) other landscapes are regolith-shielded and show little weathering response to temperature. By comparing weathering from laboratory to globe, we reconcile some aspects of kinetic and thermodynamic controls on CO_2 drawdown by natural or enhanced weathering.

Over multimillion-year time scales, the balance between weathering of silicate rocks and volcanic degassing may control the atmospheric concentration of CO_2, one of the most important greenhouse gases that regulate Earth's climate. Silicate weathering accelerates with temperature, acting as a negative feedback that buffers Earth's climate and maintains its habitability (1–5). Steps by which silicate weathering maintains Earth's low and generally stable atmospheric partial pressure of CO_2 (P_{CO_2}) include (i) production of alkalinity through solubilization of base metal cations and atmospheric CO_2 during silicate weathering, (ii) riverine transport of dissolved inorganic carbon (DIC) to the oceans, and (iii) precipitation and burial of DIC as carbonate minerals at the seafloor. Weathering of marine basalt at increased temperatures also sequesters CO_2 into minerals at the seafloor (6). In contrast to silicates, CO_2 drawn from the atmosphere during weathering of carbonate minerals is ultimately rereleased to the atmosphere. Despite the importance of the silicate weathering feedback, the mechanism of its operation is not well understood. Proposed controls vary from chemical equilibrium to kinetics to hydrology, and the sensitivity may be as low as 2% K^{-1} or perhaps as high as 20% K^{-1} [e.g., (5, 6–13)]. We explore the temperature sensitivity of weathering to understand how this feedback functions.

Although laboratory measurements might appear to be the gold standard to determine how silicate weathering varies exponentially with temperature, rates are too slow to assess accurately. Furthermore, dissolution is only one of many temperature-dependent steps that occur during weathering. Additional processes—such as solute transport, clay precipitation, biotic activity, disaggregation, fracturing, and erosion—enter systems at larger scales. These processes in turn can be influenced by climate factors such as temperature, runoff, and precipitation and by weatherability factors such as lithology, porosity, permeability, type of vegetation, and landscape position or distribution of land mass [e.g., (1, 14, 15, 16)]. Whether kinetics or equilibrium controls the temperature sensitivity remains an open question (9).

We hypothesized that combined observations from laboratories, soils, watersheds, and the globe could elucidate puzzles about weathering versus temperature. For example, researchers disagree about how chemical weathering

[1]Earth and Environmental Systems Institute, Pennsylvania State University, University Park, PA, USA. [2]Department of Geosciences, Pennsylvania State University, University Park, PA, USA.
*Corresponding author. Email: brantley@geosc.psu.edu
†These authors contributed equally to this work.

Fig. 1. Conceptual models for soils and watersheds on silicate lithologies in the humid half of Earth's land surface. (**A** to **D**) Reaction fronts [gray hachured layers in (A) and (B)] indicate where most CO_2 is solubilized during silicate weathering. For a bedrock mineral such as $CaSiO_3$, for example, weathering ($2CO_2 + H_2O + CaSiO_3 \rightarrow Ca^{2+} + 2HCO_3^- + SiO_{2(aq)}$) releases dissolved inorganic carbon that is transported, precipitated, and partially sequestered as buried carbonate minerals at the seafloor ($Ca^{2+} + 2HCO_3^- \rightarrow CO_2\uparrow + H_2O + CaCO_{3(s)}$) offshore from the landscapes in (C) and (D). In (A), kinetic limitation (KL) of silicate weathering is indicated by soil profiles or small head catchments where the silicate and its reaction front are exposed everywhere at the land surface, allowing dissolution to proceed far from equilibrium. In (B), weathering of soil profiles and watersheds characterized by buried reaction fronts for bedrock minerals instead can be dominated by flow paths where concentrations of weathering products increase until they cause dissolution to stop. Weathering fluxes from such watersheds can correlate with erosion rate, that is, they are erosive transport–limited (ETL). As shown in (C), in watersheds of increasing size (schematically shown as white teardrop shapes), the decreasing kinetic-limited landscape fraction and increasing dominance of long flow paths drive weathering fluxes to vary with erosion rate (erosive transport–limited). Only small watersheds tend to be kinetic-limited as in (A), but both small (B) and large watersheds [(C) and (D)] can be erosive transport–limited because feedbacks couple weathering fluxes to erosion rates. Thus, as watersheds become larger, they show transition regime (TR) behavior between kinetic- and erosive transport–limited landscapes.
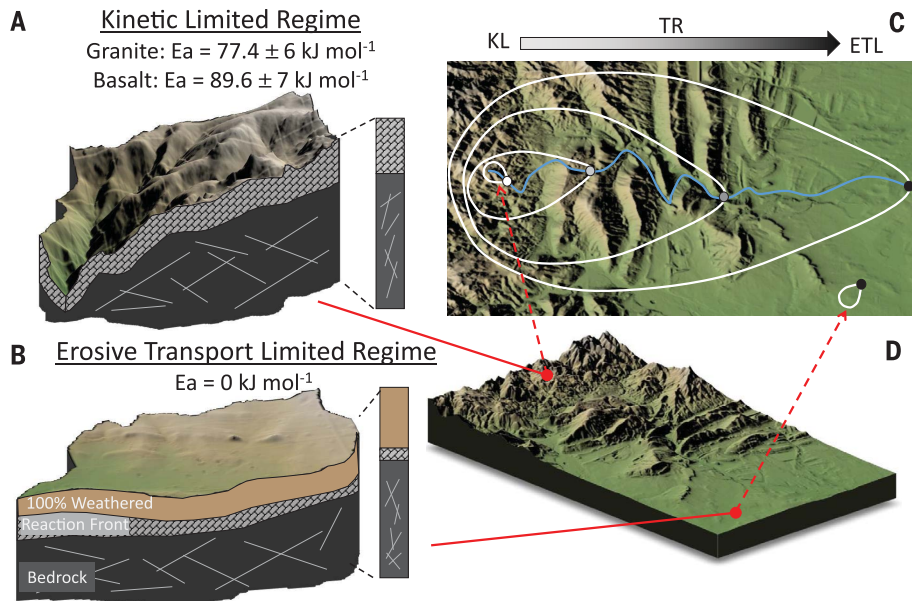
is affected by erosion, temperature, and runoff [e.g., (14, 17)], and the temperature dependences for soils and small and large watersheds do not match (4, 14, 17–20). Additional puzzles include how stream chemistry [e.g., (21)] and mountain-building events at different time scales are linked with climate, including how to explain the "Cenozoic isotope-weathering paradox" [e.g., (6, 16, 22)]. To reconcile observations, we present conceptual models at different spatial and temporal scales and emphasize feedbacks related to how the geological subsurface is structured by weathering reactions and fracturing to guide and respond to groundwater flow (23–25).

Using standard kinetic treatments, we use the Arrhenius equation (eq. S1) to express temperature sensitivity. This allows calculation of the Arrhenius activation energy, Ea, from the natural log of the relative increase in rate as temperature changes from a reference temperature, T_0, to a higher value, T (eq. S2). By using Ea, we rely on standard treatments of chemical kinetics by attempting to isolate chemical dissolution from other factors. In the "Global integration" section, we recast Ea as the percent change in weathering flux per degree temperature change globally. In contrast to previous researchers, we neither require that weathering is kinetic-limited everywhere nor require that Ea is the same at every spatial scale [e.g., (10, 26, 27)]. Instead, we assume that weathering systems can be treated with temperature-independent Ea values at each spatial scale. Although Ea might also change with temperature [e.g., (28)], our simplified treatment allows parsimonious upscaling to a global model. We discovered that Ea varies as additional processes become coupled to dissolution at higher scale. We also emphasize that kinetics can only limit the weathering of landscapes where the exposure time of rocks to weathering is short compared with the reaction time scale [i.e., (18)] and the net water balance is positive, that is, mean annual precipitation (MAP) is greater than potential evapotranspiration (PET) [i.e., (29, 30)]. With this approach, the temperature sensitivity of weathering can be reconciled across scales, yielding an approach to understand weathering in the past or in a human-manipulated future.

Analyzing Earth's thermostat

Some authors have explored controls on the long-term carbon balance by quantitatively upscaling based on exposed lithologies (31, 32). For example, global continental land area is ~63% sediments and ~35% crystalline rock, where the latter are ~15% basaltic and ~85% granitic (31). A more high-resolution assessment yielded 56.24% of exorheic land area as sediments (excluding carbonates), 24.3% crystalline rock (excluding volcanics), and 7.00% volcanics (86% basaltic) (32).

Table 1. Thermodynamic values and activation energies for kinetic-limited systems. $\Delta G°$, standard Gibbs Free Energy.

| System	$\Delta G°$ and Ea values (kJ mol^{-1})
Granite	
Albite → kaolinite in laboratory	$\Delta G° = 83.5 \pm 2$
Oligoclase → kaolinite in laboratory	$\Delta G° = 74$
Rate-limiting step is dissolution (laboratory)	
Far-from-equilibrium mineral dissolution (oligoclase)*	$Ea_{dissolution} = 67 \pm 2$
Far-from-equilibrium Na release, rock dissolution†	$Ea_{dissolution} = 57 \pm 15$
Coupled dissolution, transport, and/or clay precipitation	
Kinetic-limited soils‡	$Ea_{dissolution} = 79.8 \pm 8$
Coupled dissolution, transport, clay precipitation, fracturing, and/or erosion	
Kinetic-limited watersheds (corrected for MAP and erosion as needed)§	$Ea_{apparent} = 77.4 \pm 6$ (11.2% K^{-1})¶
Transition-regime watersheds (corrected for MAP but not erosion)#	$Ea_{apparent} = 36.1 \pm 15.2$
Theoretical prediction (eqs. S5 and S11)	
$Ea_{dissolution} < Ea_{apparent} < Ea_{diffusion} + Ea_{dissolution} + \Delta G°/3$	$Ea_{apparent} = 67$ to 110
Basalt	
Labradorite → kaolinite in laboratory	$\Delta G° = 64 \pm 7$
Rate-limiting step is dissolution (laboratory)	
Far-from-equilibrium mineral dissolution (labradorite)**	$Ea_{dissolution} = 43 \pm 1$
Si release, crystalline or glassy basalt dissolution††	$Ea_{dissolution} = 46 \pm 2$
Coupled dissolution, transport, and/or clay precipitation	
Olivine in a soil column in laboratory‡‡	$Ea_{apparent} = 72$
Solute release during rind formation on basalts	$Ea_{apparent} = 54 \pm 12$
Solute release during rind formation on andesites and basalts	$Ea_{apparent} = 64 \pm 12$
Coupled dissolution, transport, clay precipitation, fracturing, and/or erosion	
Kinetic-limited watersheds§§	$Ea_{apparent} = 89.6 \pm 7$ (13% K^{-1})¶
Transition-regime watersheds (not corrected for MAP or erosion)#	$Ea_{apparent} = 42.5 \pm 1.3$¶
Theoretical predictions (see supplementary materials)	
Rinds: $Ea_{apparent} = Ea_{diffusion} + \Delta G°/1.6$	$Ea_{apparent} = 55 \pm 7$
Soils: $Ea_{dissolution} < Ea_{apparent} < Ea_{diffusion} + Ea_{dissolution} + \Delta G°/1.6$	$Ea_{apparent} = 43$ to 98

*Weighted average of synthesized laboratory estimates of $Ea_{dissolution}$ for oligoclase in laboratory from table S1A.   †As summarized in table S1A (14).   ‡From values in table S1B, as described in the text.   §From values in table S1C, as described in the text.   ¶The fractional rate of change with temperature, α, for a given Ea approximately equals Ea/RT_0^2, where R is the universal gas constant and T is 288 K, the average Earth surface temperature (2, 3).   #Calculated for granitoids (4) and the average of basalt fluxes (61, 179).   **From table S2A.   ††Weighted average Si release rates from crystalline and glassy basalt rock in table S2A (uncorrected for Al).   ‡‡See table S2B.   §§From Icelandic rivers, as summarized in table S2B. Error is assumed to be ±1% K^{-1}.

We instead analyze a few important minerals that were chosen from those lithologies. Silicate minerals solubilize CO_2 from the atmosphere during weathering and release charged DIC species as the minerals release aqueous base metal cations (Na^+, K^+, Mg^{2+}, Ca^{2+}) with uncharged aqueous silica ($SiO_{2(aq)}$). Ca and Mg are reprecipitated as carbonates in the oceans, thereby sequestering CO_2 and balancing the CO_2 flux from volcanic degassing (1, 16) when considered at time scales greater than 10^5 to 10^6 years. By contrast, K^+ delivered to the ocean may be removed through back reactions with silicates at the seafloor, rereleasing CO_2 to the atmosphere (33). K^+ is also immobilized in soils as clays or taken up into biota in soils. A large fraction of the dissolved riverine Na^+ is exchanged with Ca^{2+} and Mg^{2+} on suspended sediments during transport to the oceans (34), and these cations in turn sequester CO_2 as (Ca,Mg)-containing carbonates at the seafloor, in effect sequestering DIC associated with Na release as carbonate sediment.

Using these observations, we review previous determinations of Ea from plots of log (reaction rate) versus T^{-1} (eqs. S1 and S2) for weathering of the common Ca-, Mg-, and Na-containing silicates that dominate basalts and granites. These include the Ca- and Mg-containing olivine and diopside minerals in basalts and Na- and Ca-containing plagioclase feldspar that is found in both basalts and granites. Plagioclase is particularly important not only because it is the most abundant
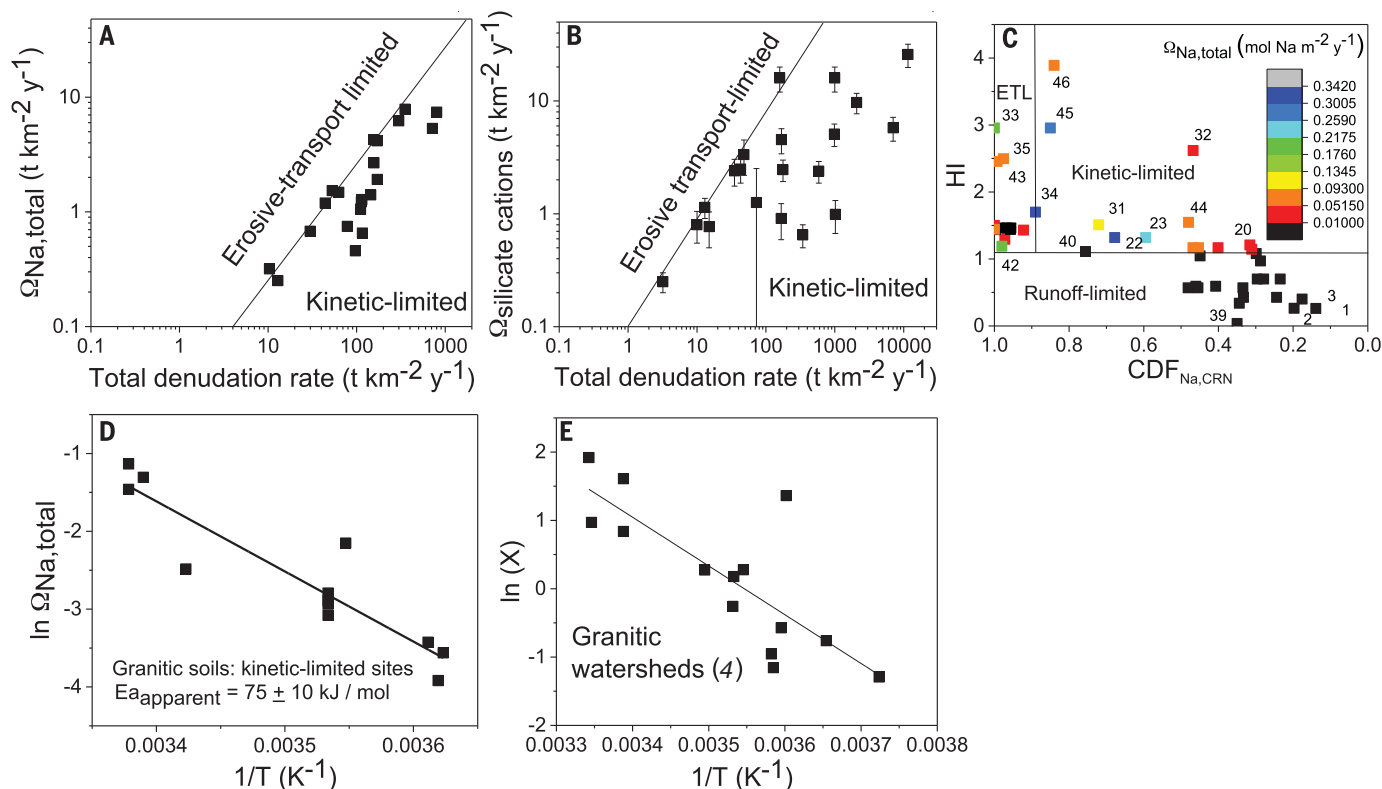
Fig. 2. Weathering rates plotted versus controlling variables. (**A**) Total Na weathering rate, $\Omega_{Na,total}$, for the granitic soils that are not runoff-limited (table S3). (**B**) Total silicate cation weathering rates, $\Omega_{cations,total}$, for erosive transport– and kinetic-limited watersheds from an earlier publication (*4*). In (A) and (B), symbols plotting on and off the line are interpreted as limited by erosive transport or kinetics, respectively, and error bars indicate estimates from the original publication (*4*). (**C**) Summary plot of all 45 soils in table S3 color coded for $\Omega_{Na,total}$ and categorized by HI and $CDF_{Na,CRN}$ (see table S3 for index numbers where indicated). The solid horizontal and vertical lines represent estimated values of HI and CDF that separate the labeled weathering regimes as discussed in the text. (**D** and **E**) Arrhenius plots for the kinetic-limited soils (table S3) (D) and watersheds (E) (*4*). *X* is a weathering rate function corrected for MAP and denudation rate by using parameters from the original authors who calculated $Ea_{apparent}$ = 74 kJ mol^{-1}. Table S3 includes sites with slopes <7.5° from an earlier publication (*18*) after reanalysis (*29*) as well as additional sites from published reports.

crustal mineral but also because it is the source of almost all Na released naturally to rivers, making the assessment of rates of plagioclase weathering from riverine chemistry more robust than that for other abundant rock-forming silicates. This assessment is further simplified because Na usually does not accumulate in biota or clays (an observation revisited in our treatment). Plagioclase feldspar is also one of the more abundant of the reactive, noncarbonate, base metal cation–releasing silicates in the sediments that cover about two-thirds of the continents (*32*).

Laboratory measurements

Comparisons of laboratory kinetics (tables S1A and S2A) reveal that activation energies of dissolution, $Ea_{dissolution}$, are highest for the Mg-releasing minerals (58 to 96 kJ mol^{-1}). For feldspars, values of $Ea_{dissolution}$ are lower and decrease with increasing Ca content from granitic to basaltic compositions. For example, oligoclase ($Ea_{dissolution}$ = 67 ± 2 kJ mol^{-1}) and labradorite ($Ea_{dissolution}$ = 42.8 ± 1 kJ mol^{-1}) are the most common feldspars in granite and basalt, respectively (Table 1).

The compilations also allow comparison of $Ea_{dissolution}$ from isolated-mineral experiments to that of the same mineral dissolved in reactors packed with other phases. For example, the $Ea_{dissolution}$ estimates for Mg-rich olivine (65.6 to 85.7 kJ mol^{-1}) from single-mineral experiments bracket $Ea_{apparent}$ for olivine dissolved in a soil column (72.5 kJ mol^{-1}) (table S2A). We call the latter an $Ea_{apparent}$ because additional steps can enter or couple with dissolution at higher scales. This can change the rate-limiting step or add an additional temperature dependence (*35*).

Similarly, the value of $Ea_{dissolution}$ for a granitic feldspar (oligoclase, 67 ± 2 kJ mol^{-1}) is within error of the $Ea_{apparent}$ that describes Na release from granitic whole-rock experiments, 57 ± 15 kJ mol^{-1} (Table 1 and table S1A), which is expected given that the dominant base metal cation released from dissolving granite is Na. Similarly, although solute release from crystalline basalt is dominated by Mg from olivine at lower pH and Ca from feldspar at higher pH (*36*), we show that the $Ea_{apparent}$ for basalt dissolution is similar to that of feldspar dissolution (table S2A). Specifically, the $Ea_{apparent}$

for Si release over a range of pH from glassy or crystalline basalt, 46 ± 2 kJ mol^{-1}, is within error of the $Ea_{dissolution}$ of labradorite (43 ± 1 kJ mol^{-1}) (Table 1 and table S2A). Given these observations, we emphasize plagioclase feldspar weathering and Na release in the next sections, which treat higher spatial scales.

Soil analysis
Granitic systems

To estimate $Ea_{apparent}$ in natural systems, Na release rates, Ω_{Na}, are assessed for sets of soils known as climosequences that span gradients in mean annual temperature (MAT) [e.g., (*18*)]. For example, a master set of 45 soils from sites such as terraces and ridgetops is summarized in table S3. These soils were chosen because (i) they generally formed on relatively homogeneous parent materials with minimal disturbance by humans or glaciers, and (ii) their chemical and physical denudation rates have been estimated. Ridgetops and terraces are considered the most straightforward to model because they are functionally one-dimensional (1D) in that water and sediments are not transported into them from upslope.

Key to the analysis is that dissolution of feldspar in a 1D soil is localized into a reaction front (e.g., Fig. 1) or depth interval where all reaction occurs [e.g., (37)]. Below the front, pore fluids generally flow more slowly and are sufficiently concentrated so that they react only minimally with feldspar. At any depth in such a 1D profile, the fraction of mineral depleted by weathering can be estimated compared with the parent rock concentration. This depth-dependent fraction, termed the chemical depletion fraction (CDF; estimated from eq. S4), varies from zero in the parent material to values ≤100% above or at the top of the front. The error in CDF is larger in soils when CDF is small and in regions of substantial dust additions or parent composition variability.

Profiles with 0 < CDF < 100% for a dissolving mineral at the land surface (i.e., Fig. 1A) are "incompletely developed" because they retain the mineral throughout the weathering column. When such profiles are identified for plagioclase feldspar, exposure times (for non-eroding soils) or residence times (for eroding soils) are inferred to be short compared with the time scale of plagioclase dissolution (37). Instead of concentrations of plagioclase, however, Na is measured as a proxy because most Na in granitic material is typically in feldspar. We also assume for eroding 1D soils that the erosion rate and weathering advance rate are roughly balanced (expressed in units of length per time), which explains why soils endure and can remain roughly constant in thickness over the soil residence time. With those assumptions, mass balance arguments show that CDF values calculated at the land surface for Na, $CDF_{Na,surf}$, equal the fraction of the total denudation rate (D, in tonnes km^{-2} $year^{-1}$) of Na caused by chemical weathering (18). For example, $CDF_{Na,surf}$ = 100% implies 100% chemical removal of plagioclase and negligible loss to erosion (Fig. 1A). The implication from models is that incomplete (0 < $CDF_{Na,surf}$ < 100%) or complete development of a 1D profile ($CDF_{Na,surf}$ = 100%) reflects kinetic or erosive-transport limitation of plagioclase weathering, respectively (37).

For most soils in table S3, weathering release rates of Na were calculated from $CDF_{Na,surf}$ by following approaches based on cosmogenic radionuclide (CRN) concentrations (18). This approach yields Na release rates, $\Omega_{Na,CRN}$, calculated as the product of the denudation rate, D_{CRN}, multiplied by $CDF_{Na,CRN}$ and $[Na]_{rock}$ (18). The subscript CRN is used because $CDF_{Na,CRN}$ and D_{CRN} are the $CDF_{Na,surf}$ and denudation rate, respectively, averaged over the surficial layer of soil where penetration of cosmic rays result in accumulation of CRN. $[Na]_{rock}$ is the Na concentration of bedrock. Later treatments (29) corrected these rates to include weathering in saprolite below the layer of CRN accumula-
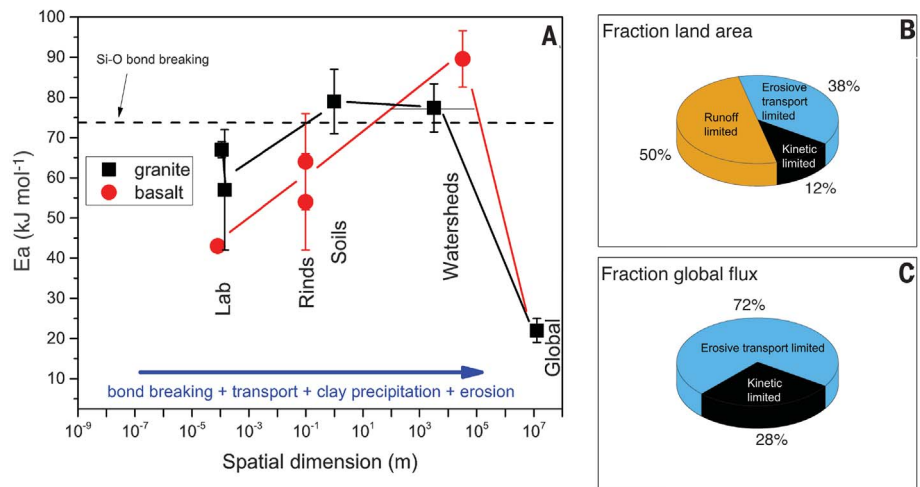
Fig. 3. Global assessment of *Ea* across spatial scales. (A to C) Variation in *Ea* for kinetic-limited weathering from laboratory to rind formation to soils to watersheds. Weathering mechanisms include additional steps as the spatial dimension increases from ~100-μm mineral grains to ~10-cm clasts to ~1-m soils to ~10^2- to 10^5-m drainage basins. The calculated *Ea* of bond breaking of an edge site for tetrahedral silicate anions is shown as 74 kJ mol^{-1}. The calculated *Ea* for silicate weathering for the global Earth was not upscaled based on fractional land areas of weathering regimes (B) but instead on fractional contributions of fluxes (C). First, a temperature response was estimated based on the relative proportions of global CO_2 consumption fluxes from the two main lithologies, granite (74%) and basalt (26%) (11.7% K^{-1}). This was then used to upscale *Ea* to the globe based on the proportions from each weathering regime (C) where the contribution from runoff-limited watersheds was assumed to be negligible. Symbols in (A) show averages with 1σ from Table 1, where the laboratory symbols represent oligoclase or rock (granite) and labradorite (basalt); the two rind symbols represent basaltic and andesitic-basaltic compositions. See text for further explanations.

tion (38). We refer to these corrected weathering and denudation rates for Na as $\Omega_{Na,total}$ and $D_{Na,total}$, respectively (see table S3).

To calculate $Ea_{apparent}$ for weathering, we focused on 1D granitic soils that are incompletely developed with respect to Na because such soils are often kinetic-limited, and that weathering regime is the only one that we expect to show strong temperature sensitivity (18). Completely developed soils (90% ≤ $CDF_{Na,CRN}$ ≤ 100%) were not considered on the assumption that they are limited by erosion rate rather than kinetics and therefore are not strongly dependent on MAP or MAT (fig. S3): Such fluxes for soils listed in table S3B plot on the line in Fig. 2A. The threshold CDF for completely developed profiles was dropped from 100 to 90% because $CDF_{Na,CRN}$ generally is only known to about ±10% (35). This threshold also allowed identification of one soil as erosive transport–limited rather than kinetic-limited, which is consistent with its extreme weathering depth (table S3B).

We also did not consider soils with incompletely developed reaction fronts for feldspar in calculations of $Ea_{apparent}$ when they developed under a negative local water budget. For such soils, weathering appears limited by lack of water flushing instead of by weathering kinetics (29). Na reaction fronts in some of these soils extend to great depths, but Na is

nonetheless retained at the land surface. This occurs in some cases because of the precipitation of Na-containing smectitic clays (39). We refer to this dry regime as limitation by runoff, where runoff is equated to MAP minus PET.

To identify runoff limitation, we could not rely on clay compositions or depth of total weathering because these were not always reported for the soils listed in table S3. We followed an earlier approach (29) and calculated the approximate threshold for runoff limitation as the point where the humidity index (HI), defined as MAP divided by PET, falls below unity. But errors in MAP and PET make this threshold very approximate: For example, a value of unity did not allow inclusion of a soil with a deep, incompletely developed Na profile (table S3A) where smectite, a geologically long-term indicator of retention of base metal cations (35), had been reported. That site, characterized by HI = 1.1, has a relatively high MAP with a very long dry season. To include that soil in the regime of runoff limitation, we set the threshold HI at 1.1.

Clearly, such ad hoc definitions for runoff limitation are potentially problematic, but the small number of soils with $\Omega_{Na,total}$ estimates based on the CRN approach (table S3) precludes rigorous testing. In addition, runoff limitation has not been investigated as a

regime of weathering by most authors, despite the acknowledged importance of runoff [e.g., (4, 20, 29)]. We therefore further tested the idea of runoff limitation as a function of HI by investigating watershed data. We focused on a commonly measured weathering-derived solute (SiO_2) and assessed silica release rates, Ω_{SiO2}, versus runoff (defined here as stream discharge normalized by basin area). To simplify our analysis to only hypothetically kinetic- and runoff-limited watersheds, we targeted watersheds on highly erodible shale, assuming that few shales would weather in the erosive transport–limited regime (35). Validating expectations for runoff and kinetic limitation, respectively, shale-derived Ω_{SiO2} data are strongly runoff-dependent at low HI and highly temperature-dependent at high HI (fig. S2, D and F). Given that Ω_{SiO2} is determined from concentration (C) times discharge (q) normalized by basin area (35), a linear dependence of Ω_{SiO2} on runoff (fig. S2E) implies that C is independent of q (fig. S2H). Figure S2H highlights the possibility that such discharge-independent or "chemostatic" (21) concentrations in low-HI watersheds could reflect smectite-kaolinite equilibration. This reaction could also explain why low-HI SiO_2 fluxes do not generally increase with temperature (fig. S2F). Specifically, the stoichiometry and negative enthalpy of this reaction require that concentrations of SiO_2 decrease as the equilibrium shifts toward smectite with increasing temperature.

To determine the temperature sensitivity of weathering for the 45-soil dataset, we therefore eliminated both runoff- and erosive-transport limited sites by using HI and CDF criteria, respectively, and focused on the 12 remaining kinetic-limited soils (table S3C). We also considered temperature correlations for MAP and $D_{Na,total}$ for the 12 soils. Such correlations occur because precipitation increases with temperature over broad spatial scales [e.g., (40)] and because chemical weathering is coupled to physical erosion (18). We used a power-law treatment to explore if $\Omega_{Na,total}$ should be corrected for such correlations. That treatment (eq. S3c) had previously been used to correct values of $\Omega_{Na,CRN}$ for MAP and D_{CRN} (18), yielding an $Ea_{apparent}$ equal to 17 kJ mol^{-1}, which is much lower than the $Ea_{dissolution}$ for plagioclase (Table 1). However, with that "correction," much of the temperature dependence in $\Omega_{Na,CRN}$ was effectively attributed to denudation because, counter to expectations for kinetic limitation, $CDF_{Na,CRN}$ shows little variation with denudation. We similarly observed such a lack of variation in $CDF_{Na,CRN}$ with $D_{Na,total}$ (fig. S4A), but we embraced the alternate interpretation posed by the researchers (18), namely, that $\Omega_{Na,CRN}$ correlates with denudation because erodibility increases as chemical weathering weakens and disaggre-

gates rock [e.g., (41, 42)]. We also argue (35) that error in CDF obscures variations with denudation in some but not all fast-eroding systems (18, 43).

Instead of following the earlier approach (18), we therefore attributed the temperature dependence of denudation to the $Ea_{apparent}$ of weathering and its effect on rock disintegration into blocks or particles. Without using the power-law correction, $Ea_{apparent}$ for the 12 soils in table S3C equals 75 ± 10 kJ mol^{-1} (Fig. 2D). Corroborating this value are three other estimates between 75 ± 14 and 112 ± 34 kJ mol^{-1} from two additional kinetic-limited climosequences on loess and shale (table S1B), where measurements of concentrations to depths of meters removes some but not all ambiguities in CDF_{Na} (35). Corrections for MAP and $D_{Na,total}$ are considered irrelevant on the loess and shale because MAP and $D_{Na,total}$ vary negligibly or are temperature-independent. The weighted average of all the estimates, 79.8 ± 8 kJ mol^{-1} (Table 1), is considered our best estimate of granitic soil–based $Ea_{apparent}$.

Basaltic systems

No soil-based estimates of Ea describe the weathering of basaltic soils based on CRNs. Instead, 13 reports of weathering rind formation on basalts or the less Mg-rich andesites were found with HI > 1.1 along with a few measurements of pitting on naturally exposed basaltic feldspars (tables S2B, S4, and S5). For these, rind formation initiates as plagioclase alters to clay. For HI > 1.1, the best estimate of $Ea_{apparent}$ for rind formation equals 54 ± 12 kJ mol^{-1} for basalts and 64 ± 12 kJ mol^{-1} for basalts and andesites (35). These values overlap with the range of $Ea_{apparent}$ that was estimated for one study of porosity development on naturally exposed basaltic plagioclase, 56 ± 16 to 97 ± 10 kJ mol^{-1} (table S2B).

Watershed analysis
Granitic systems

In this section, we analyze watershed studies that report $Ea_{apparent}$. The published studies for granitic watersheds (table S1C) focus on Na, Si, or base metal–cation release rates corrected for nonsilicate-derived cations. As expected for studies that mostly emphasize permanent streams, almost all $Ea_{apparent}$ estimates are for systems at relatively high HI. This partly explains why runoff limitation has not been defined previously for watersheds [however, see (4, 20, 21)]. Separation of runoff-limited watersheds is nonetheless important because only the analysis of high-HI watersheds yields an $Ea_{apparent}$ value that is significant (fig. S2F).

To calculate a best estimate of $Ea_{apparent}$ for watersheds to compare with that of other spatial scales, we focused on Na or carbonate-corrected silicate cation release rates ($\Omega_{Na,total}$ or $\Omega_{cations,total}$, respectively). Treating these

fluxes together relies on the assumption that their $Ea_{apparent}$ values are comparable because feldspars dominate granitic cation release. We did not include Ω_{SiO2} because Si-based $Ea_{apparent}$ is consistently lower for watersheds where release rates of cations and Si are both reported (table S1C). As for soils, we also considered potential temperature correlations for MAP and D. In some cases, these correlations were not observed. For example, in one compiled dataset from >40 head catchments, values of $\Omega_{Na,total}$ were corrected for MAP but not denudation because $\Omega_{Na,total}$ showed no variation with a proxy for erosion (relief) (44). Three other studies targeted only a few neighboring watersheds, negating the need for regional corrections of MAP or denudation. The fifth study (see Fig. 2, B and E) corrected $\Omega_{cations,total}$ for 13 alpine or montane watersheds for both MAP and D_{total} by fitting $\Omega_{cations,total}$ to a version of power-law eq. S3c, yielding $Ea_{apparent}$ = 74 ± 29 kJ mol^{-1} (4). The weighted average of these watershed $Ea_{apparent}$ values for granites equals 77.4 ± 6 kJ mol^{-1}.

Before accepting this estimate, however, we address an apparent contradiction. Specifically, we used watershed values of Ω that were corrected for MAP and D (4) by fitting to the same power-law equation (18) that we rejected for soils. The fit [see also (45)] showed that the chemical weathering correlation with total denudation is weaker for watersheds (power-law exponent a < 1) than soils (a ≈ 1) (4). But in addition, the fits differ in that the correction for D for soils lowers the $Ea_{apparent}$ (compared with its uncorrected value), whereas the correction for watersheds increases $Ea_{apparent}$. We explore this difference next using Fig. 1.

In Fig. 1A, we propose that kinetic-limited watersheds are like kinetic-limited soils in that they retain feldspar at the surface. However, in watersheds, the soils are not the only factor that dictates stream chemistry. Conceptually, release rates of silicate-derived cations such as Na are kinetic-limited only in watersheds that are small enough that ground waters flowing from soil to stream cumulatively interact with little feldspar. Short flow paths and residence times preclude the attainment of chemical equilibrium [see, for example, (46)]. The result is that long-term average stream concentrations in kinetic-limited watersheds vary with discharge because each flow path is limited by temperature-dependent kinetics ($Ea_{apparent}$ ≈ 80 kJ mol^{-1}) and not by equilibrium.

The other type of head catchment is characterized by feldspar-absent topsoils (Fig. 1B) and stream concentrations that are more likely to be roughly constant (chemostatic) as a function of variable discharge when observed over years to decades. Because water chemistry is unlikely to equilibrate with feldspar at ambient conditions even for long flow paths (47), this

chemostasis could reflect a limiting reagent in the dissolving waters, steady-state concentrations that are dictated by the dissolution of primary minerals balanced by precipitation of secondary minerals, or equilibration among secondary minerals [e.g., (5, 21, 48, 49)]. But for small granitic watersheds similar to that shown in Fig. 1B, it has been observed that their weathering fluxes vary strongly with erosion rate rather than temperature [e.g., (15)]. For this reason, we label them erosive transport–limited and assume $Ea_{apparent} \approx 0$ kJ mol^{-1}.

As watersheds become larger (Fig. 1C), they are increasingly dominated by lowlands [e.g., (20)] and by chemostatic behavior because groundwater flow paths become deeper, longer, and more likely to interact with feldspar for extended residence times [e.g., (46)]. But large watersheds are similar to the watersheds in Fig. 1B in that their weathering fluxes are observed to depend strongly on erosion rate and not temperature [e.g., (20)]. The fluxes of these large watersheds are thus considered erosive transport–limited: The average product of flow-weighted C and q depends on erosion rate (20).

Returning to the power-law corrections for Ω, we argue that fitting watersheds using eq. S3c adjusts for the fraction of soil landscapes and flow paths that are kinetic-limited ($Ea_{apparent} \approx 80$ kJ mol^{-1}) versus erosive transport–limited (~0 kJ mol^{-1}). Although the large watersheds may contain kinetic-limited headwater catchments, these do not dominate mainstem chemistry downstream. The power-law correction to calculate temperature sensitivity of weathering thus yields a higher, rather than lower, $Ea_{apparent}$. Two corollaries to this argument can be tested. First, if this argument is defensible, then the maximum weathering fluxes for aggregated datasets for soils and watersheds should be similar. This has been documented (4, 50) (see also Fig. 2). The second corollary is that virtually all kinetic-limited watersheds should be small, whereas erosive transport–limited watersheds should be both large and small. This has also been observed (4, 50).

But, why should averaged fluxes (= $C \cdot q$) from erosive transport–limited watersheds tend toward values dictated by erosion rate? The most likely answer is feedbacks that couple water chemistry, subsurface flow paths, fracturing, and erosion at the watershed scale. For example, permeability changes driven by weathering and fracturing [e.g., (23, 51)] could comprise feedbacks that couple weathering flux to erosion. Some aspects of such feedbacks have been explored for pyrite weathering (24, 25). Processes related to vegetation are also potential feedbacks [e.g., (52)].

Basaltic systems

The reported values of $Ea_{apparent}$ for basaltic watersheds ranged as high as 89.6 kJ mol^{-1} (table S2B). That value derives from an $Ea_{apparent}$ for Icelandic volcanic watersheds after correction for runoff and glacial melting (53). Conversely, the Icelandic fluxes were not corrected for issues related to carbonates formed from volcanic CO_2 (54). Those types of complications, including deep subsurface weathering and volcanic degassing [e.g., (55)], led one set of researchers to estimate global CO_2 consumption for basalts by focusing only on 22 inactive volcanic systems (table S2B). Their calculated $Ea_{apparent}$, which was much lower than the Icelandic value, was similar in magnitude to an earlier estimate based on 10 systems (table S2B). No evidence requiring a correction for runoff, MAP, or denudation rate was reported in either study. Weighting and averaging the two lower values yields 42.5 ± 1.3 kJ mol^{-1} (table S2B).

To reconcile these high and low values, we propose, by analogy to granitic watersheds, that the higher $Ea_{apparent}$, 89.6 ± 7 kJ mol^{-1}, for the Icelandic systems (19, 53) is the best estimate for kinetic-limited basaltic landscapes and the lower value, 42.5 ± 1.3 kJ mol^{-1}, reflects contributions from both kinetic- and erosive transport–limited soils within transition-regime watersheds (Fig. 1). As summarized in table S2B, the higher $Ea_{apparent}$ corroborates previous treatments of cross-scale weathering that yielded 70 ± 20 kJ mol^{-1} (26) and seafloor basalt weathering based on inverse modeling that yielded 75 ± 22 to 92 ± 7 kJ mol^{-1} (6, 12). Likewise, values of $Ea_{apparent}$ that range as high as 109 kJ mol^{-1} have been reported from the pitting of naturally exposed plagioclase grains (table S2B).

Cross-scale comparison

Many additional lines of evidence confirm aspects of these interpretations. For example, molecular calculations of Ea of hydrolysis of Si tetrahedral networks at edges or corners on Na feldspar surfaces, 74 to 120 kJ mol^{-1} (56), are slightly higher than the laboratory $Ea_{dissolution}$ values (43 to 67 kJ mol^{-1}), probably because of proton sorption (57). If we invoke arguments related to differences in Al content (56), molecular calculations are also consistent with the laboratory-based conclusion that $Ea_{dissolution}$ values for the dominant granitic feldspars are higher (67 kJ mol^{-1}) than those for basaltic feldspars (43 kJ mol^{-1}).

The laboratory values of $Ea_{dissolution}$ for the Na- and Ca-feldspars are within error of the values for granite and basalt whole-rock dissolution, respectively, but the $Ea_{apparent}$ values increase by at least 10 kJ mol^{-1} or as much as 50 kJ mol^{-1} for soils formed on granite and for watersheds formed on basalts, respectively (Table 1 and Fig. 3). Biota might cause this lab-field difference because we know very little about the biotic effects on Ea (tables S1 and S2). However, where biotic effects have been measured, they sometimes decrease rather than increase the $Ea_{apparent}$ (tables S1A and S2, A and B), and neither biota nor types of land cover are reported in recent studies as major factors that control weathering rates in watersheds (7, 58). The biotic effect may be small and largely caused by pH because organic acids are low in concentration in soils (59). We averaged Ea values across pH ranges where measurements were made.

Instead, we argue that this ~10 kJ mol^{-1} (granite) or 50 kJ mol^{-1} (basalt) laboratory-field discrepancy arises because feldspar weathering in the laboratory is studied far from equilibrium and depends strictly on dissolution, whereas the mechanism in natural systems includes contributions from processes that enter at higher spatial scales and that cannot be entirely separated, including transport, precipitation of clays, rock disaggregation, and fracturing (25). For example, theoretical predictions for dissolution-precipitation coupling (eqs. S11, S17, and S18) may explain the value for both granites and basalts (Table 1). Likewise, researchers have argued that the high $Ea_{apparent}$ for Icelandic basalts reflects dissolution and secondary mineral precipitation (53). The inextricable coupling of erosion and chemical weathering [e.g., (15, 18, 20)] also points to temperature-sensitive processes such as disaggregation or subsurface flow partitioning that contribute to soil- or watershed-based $Ea_{apparent}$ values.

Global integration

Assuming that these approaches to treating chemical weathering, physical denudation, and hydrology are defensible, we now upscale to the global system by calculating the fractional change in silicate weathering flux with each degree increase in temperature, α_{sw}, for the kinetic-limited regime using the approximation that $\alpha_{sw} \approx \frac{Ea}{RT_0^2}$ (2, 3), where R is the universal gas constant. After setting T_0 to the global mean temperature of 288 K, the values of α_{sw} equal 11.2 and 13% K^{-1} for kinetic-limited granitic and basaltic catchments (Table 1), respectively.

To upscale requires assessing α_{sw} for global distributions of lithology and weathering regime. Instead of upscaling for lithology by area, however, we instead upscaled using proportions of CO_2 consumption flux as a function of lithology. This strategy reflects that the fractional areas for each lithology do not translate directly to the proportion of flux because of uneven geographic distributions of lithology and MAP [e.g., (32, 60)]. To upscale, we note that the CO_2 consumption flux from basaltic weathering is estimated based on rivers as 16.5 to 35% (average = 26%) of the total global silicate CO_2 consumption flux (20, 32, 61). Based on this, we calculated the lithologic flux-weighted α_{sw} of 11.7% K^{-1} from the sum of the granitic

[(100% − 26%) × (11.2% K^{-1})] and basaltic terms [26% × (13% K^{-1})].

A second aspect of the upscaling is assessing the proportions of fluxes for soils in the three weathering regimes. A recent analysis (30) suggests that the fraction of global landscape with an HI less than the threshold we defined for runoff limitation is 0.496 (35). This means that half the land surface is wet and half dry or that half is fast-weathering and half is slow-weathering [see, for example, figure 6 of (32)]. To subdivide the fast-weathering wet half into kinetic- and erosive transport–limited fractions, we note that only about 9 to 14% (average ≈ 12%) of the exorheic land surface contributes 38 to 50% (average = 44 ± 6%) of the total global chemical denudation (32, 45, 62). This global CO_2 consumption flux from ~12% of the continental area is considered here to represent kinetic limitation because such watersheds tend to weather at the fastest rates (e.g., Fig. 2C) (50). However, only 63% of the global flux is from silicates, whereas the rest is from carbonates (32). Therefore, although the global fractions of land areas that are kinetic-, runoff-, and erosive transport–limited are about 12, 50, and 38%, respectively, the global fractions of flux from silicates in each regime are about 28(±4)% [= 0.63 · (0.44 ± 0.06)], 0%, and 72% respectively (Fig. 3, B and C). A simple estimate for $\frac{Ea}{RT_0^2}$ for global CO_2 consumption flux from silicate weathering based on the global lithology-weighted average α_{sw} of 11.7% therefore equals ~3.2% K^{-1} [= 28(±4)% · 0.117]. Allowing the fraction of kinetic-limited flux to vary from 38 to 50% yields an $Ea_{apparent}$ value of 22 ± 3 kJ mol^{-1}. We have assumed that (i) weathering of erosive transport–limited landscape depends only on erosion rate, (ii) the weathering flux from runoff-limited landscape is a negligible fraction of the global CO_2 consumption flux, and (iii) weathering of kinetic-limited landscape depends only on temperature. This latter assumption emphasizes that variations of chemical weathering (Ω) with MAP or runoff can be poorly handled by simple regression equations (e.g., eq. S3), given the threshold behavior we identified for chemical weathering versus HI. In that regard, our estimate is probably a lower limit. For example, if we assume that the flux from the kinetic-limited landscape responds to temperature by 11.7% K^{-1} but also to runoff increases driven by regional rises in temperature at 2.7% K^{-1} (40), then the $Ea_{apparent}$ increases to 28 kJ mol^{-1}.

Our model emphasizes that high proportions of the globe are soil-shielded or very dry, where weathering is temperature-insensitive or negligible, respectively. Even though weathering of drylands could increase with increases in MAP from warming, their minimal weathering fluxes preclude large contributions to global weathering. Our estimate of 22 ± 3 kJ mol^{-1} is within the range of values inferred from inverse

arguments based on recent global paleoclimate models (table S1C) [e.g., (12, 63)]. Those low sensitivities were required within the paleo-reconstruction models to reproduce reasonable atmospheric P_{CO_2} levels. Our model is also consistent with previous assertions about mountain-building episodes, where uplift can simultaneously focus precipitation on and exhume previously runoff-limited or shielded landscape [e.g., (64)]. After the India-Asia collision during the Tertiary, for example, the Himalayan uplift not only exposed new mineral surface and source rocks [e.g., (65)] to weathering but also redistributed precipitation locally. With such "teleconnections," CO_2 consumption fluxes could have remained near-constant globally, maintaining a balanced carbon budget (16). But if newly uplifted landscape was no longer dry or soil-shielded and instead became kinetic-limited, then the net global sensitivity of weathering to temperature could have increased, leading to a more stable climate system [see also (5)].

However, our treatment mostly explains some contradictions in the literature while emphasizing the importance of scale and runoff limitation. These factors of scale and runoff highlight a need for paleogeographic reconstructions in assessing long-term temperature sensitivity [e.g., (60)]. We also need to consider such factors if we try to enhance weathering for atmospheric CO_2 drawdown. Mining, grinding, and amending global soils with basalt (66) might accelerate weathering into the future but will be most successful if water flow is high enough and pathways short enough to remain in the regime of kinetic limitation. More attention should also focus on understanding factors such as pore-water chemistries, clays, particle sizes, fractures, biotic effects, and sub-surface flow paths that couple physical and chemical weathering during natural or enhanced weathering.

REFERENCES AND NOTES

1. T. Volk, *Am. J. Sci.* **287**, 763–779 (1987).
2. R. A. Berner, *Am. J. Sci.* **294**, 56–91 (1994).
3. B. P. C. Hayworth, B. J. Foley, *Astrophys. J. Lett.* **902**, L10 (2020).
4. A. J. West, A. Galy, M. Bickle, *Earth Planet. Sci. Lett.* **235**, 211–228 (2005).
5. K. Maher, C. P. Chamberlain, *Science* **343**, 1502–1504 (2014).
6. L. A. Coogan, S. E. Dosso, *Earth Planet. Sci. Lett.* **415**, 38–46 (2015).
7. K. Deng, S. Yang, Y. Guo, *Nat. Commun.* **13**, 1781 (2022).
8. H. C. Urey, *The Planets, Their Origin and Development* (Yale Univ. Press, 1952).
9. M. J. Winnick, K. Maher, *Earth Planet. Sci. Lett.* **485**, 111–120 (2018).
10. J. C. G. Walker, P. B. Hays, J. F. Kasting, *J. Geophys. Res.* **86**, 9776–9782 (1981).
11. R. J. Graham, R. Pierrehumbert, *Astrophys. J.* **896**, 115 (2020).
12. J. Krissansen-Totton, D. C. Catling, *Nat. Commun.* **8**, 15423 (2017).
13. P. V. Brady, *J. Geophys. Res.* **96**, 18101–18106 (1991).
14. A. F. White et al., *Geochim. Cosmochim. Acta* **63**, 3277–3291 (1999).
15. R. Millot, J. Gaillardet, B. Dupre, C. J. Allegre, *Earth Planet. Sci. Lett.* **196**, 83–98 (2002).
16. L. Kump, M. A. Arthur, in *Tectonic Uplift and Climate Change*, W. F. Ruddiman, Ed. (Springer, 1997), pp. 400–427.
17. Y. Huh, G. Panteleyev, D. Babich, A. Zaitsev, J. M. Edmond, *Geochim. Cosmochim. Acta* **62**, 2053–2075 (1998).
18. C. S. Riebe, J. W. Kirchner, R. C. Finkel, *Earth Planet. Sci. Lett.* **224**, 547–562 (2004).
19. S. R. Gislason et al., *Earth Planet. Sci. Lett.* **277**, 213–222 (2009).
20. J. Gaillardet, B. Dupre, P. Louvat, C. J. Allegre, *Chem. Geol.* **159**, 3–30 (1999).
21. S. E. Godsey, J. Hartmann, J. W. Kirchner, *Hydrol. Processes* **33**, 3056–3069 (2019).
22. M. E. Raymo, W. F. Ruddiman, *Nature* **359**, 117–122 (1992).
23. S. L. Brantley et al., *Geomorphology* **277**, 100–117 (2017).
24. A. R. Shaughnessy, X. Gu, T. Wen, S. L. Brantley, *Hydrol. Earth Syst. Sci.* **25**, 3397–3409 (2021).
25. X. Gu, P. J. Heaney, F. D. A. A. Reis, S. L. Brantley, *Science* **370**, eabb8092 (2020).
26. A. Navarre-Sitchler, S. L. Brantley, *Earth Planet. Sci. Lett.* **261**, 321–334 (2007).
27. S. A. Banwart, A. Berg, D. J. Beerling, *Global Biogeochem. Cycles* **23**, GB4013 (2009).
28. J. Lloyd, J. A. Taylor, *Funct. Ecol.* **8**, 315–323 (1994).
29. J. Rasmussen et al., *Earth Planet. Sci. Lett.* **301**, 521–530 (2011).
30. S. Calabrese, A. Porporato, *Environ. Res. Commun.* **2**, 085005 (2020).
31. P. Amiotte Suchet, J.-L. Probst, W. Ludwig, *Global Biogeochem. Cycles* **17**, 1038 (2003).
32. J. Hartmann, N. Jansen, H. H. Durr, S. Kempe, P. Kohler, *Global Planet. Change* **69**, 185–194 (2009).
33. F. T. Mackenzie, R. M. Garrels, *Am. J. Sci.* **264**, 507–525 (1966).
34. F. L. Sayles, P. C. Mangelsdorf Jr., *Geochim. Cosmochim. Acta* **41**, 951–960 (1977).
35. Materials and methods are available as supplementary materials.
36. S. Gudbrandsson, D. Wolff-Boenisch, S. R. Gislason, E. H. Oelkers, *Geochim. Cosmochim. Acta* **75**, 5496–5509 (2011).
37. M. I. Lebedeva, R. C. Fletcher, S. L. Brantley, *Earth Surf. Process. Landf.* **35**, 508–524 (2010).
38. J. I. Dixon, A. M. Heimsath, R. Amundson, *Earth Surf. Process. Landf.* **34**, 1507–1521 (2009).
39. Y. Tardy, *Chem. Geol.* **7**, 253–271 (1971).
40. M. P. Byrne, P. A. O'Gorman, *J. Clim.* **28**, 8078–8092 (2015).
41. G. Dolui, S. Chatterjee, N. Das Chatterjee, *Model. Earth Syst. Environ.* **2**, 132 (2016).
42. B. P. Murphy, J. P. L. Johnson, N. M. Gasparini, L. S. Sklar, *Nature* **532**, 223–227 (2016).
43. I. J. Larsen et al., *Science* **343**, 637–640 (2014).
44. A. F. White, A. E. Blum, *Geochim. Cosmochim. Acta* **59**, 1729–1747 (1995).
45. I. J. Larsen, D. R. Montgomery, H. M. Greenberg, *Geology* **42**, 527–530 (2014).
46. K. Maher, *Earth Planet. Sci. Lett.* **294**, 101–110 (2010).
47. C. Zhu et al., *Geochim. Cosmochim. Acta* **271**, 132–153 (2020).
48. L. Li et al., *Earths Futur.* **10**, e2021EF002603 (2022).
49. D. E. Ibarra et al., *Geochim. Cosmochim. Acta* **190**, 265–293 (2016).
50. J. L. Dixon, F. von Blanckenburg, *C. R. Geosci.* **344**, 597–609 (2012).
51. X. Gu et al., *Proc. Natl. Acad. Sci. U.S.A.* **117**, 18991–18997 (2020).
52. R. Amundson, A. Heimsath, J. Owen, K. Yoo, W. E. Dietrich, *Geomorphology* **234**, 122–132 (2015).
53. E. S. Eiriksdottir, S. R. Gislason, E. H. Oelkers, *Geochim. Cosmochim. Acta* **107**, 65–81 (2013).
54. M. G. Andrews, A. D. Jacobson, *Geochim. Cosmochim. Acta* **215**, 247–262 (2017).
55. S. Rad, K. Rive, C. J. Allegre, *Aquat. Geochem.* **17**, 221–241 (2011).
56. L. J. Criscenti, J. D. Kubicki, S. L. Brantley, *J. Phys. Chem. A* **110**, 198–206 (2006).
57. S. Nangia, B. J. Garrison, *Mol. Phys.* **107**, 831–843 (2009).
58. F. von Blanckenburg et al., *Am. J. Sci.* **321**, 1111–1163 (2021).
59. O. S. Pokrovsky, L. S. Shirokova, S. A. Zabelina, G. Jordan, P. Benezeth, *NPJ Mater. Degrad.* **5**, 51 (2021).
60. Y. Goddéris, Y. Donnadieu, G. Le Hir, V. Lefebvre, E. Nardin, *Earth Sci. Rev.* **128**, 122–138 (2014).

61. C. Dessert, B. Dupre, J. Gaillardet, L. Francois, C. Allegre, *Chem. Geol.* **202**, 257–273 (2003).
62. J. D. Milliman, K. L. Farnsworth, *River Discharge to the Coastal Ocean: A Global Synthesis* (Cambridge Univ. Press, 2011).
63. T. D. Herbert *et al.*, *Science* **377**, 116–119 (2022).
64. P. Maffre *et al.*, *Earth Planet. Sci. Lett.* **493**, 174–185 (2018).
65. J. K. Willenbring, F. von Blanckenburg, *Nature* **465**, 211–214 (2010).
66. D. J. Beerling *et al.*, *Nature* **583**, 242–248 (2020).

License information: Copyright © 2023 the authors, some rights reserved; exclusive licensee American Association for the Advancement of Science. No claim to original US government works. https://www.science.org/about/science-licenses-journal-article-reuse

SUPPLEMENTARY MATERIALS

science.org/doi/10.1126/science.add2922
Materials and Methods
Supplementary Text
Figs. S1 to S4
Tables S1 to S5
References (*67–210*)